Nuclear Inst. and Methods in Physics Research, A 901 (2018) 21–31

Contents lists available at ScienceDirect

Nuclear Inst. and Methods in Physics Research, A

journal homepage: www.elsevier.com/locate/nima

Numerical study of the thermal performance of the CERN Linac3 ion source miniature oven

C. Fichera [a,*], F. Carra [a], D. Küchler [a], V. Toivanen [b]

[a] European Organization for Nuclear Research (CERN), Geneva, Switzerland
[b] Grand Accélérateur National d'Ions Lourds (GANIL), Caen Cedex, France

ARTICLE INFO

Keywords:
Linear accelerator
Accelerator equipment design
CERN
Finite elements method
Numerical thermal analysis
Heat transfer

ABSTRACT

The Linac3 ion source at CERN produces lead ion beams by the vaporization of solid samples inside the internal ovens and the consequent ionization of the evaporated material in the plasma. The geometry, materials and surface state of the oven elements are critical parameters influencing the oven temperature characteristics and consequently the evaporation properties and the ion source performance. A dedicated test stand was assembled and a finite element approach is proposed to evaluate the thermal response of the system at increasing heating powers. Comparisons between the simulation results and experimental measurements are given in order to validate the numerical model. Radiation was found to be the main heat transfer mechanism governing the system. Based on the obtained results, improvements to the existing setup are analysed.

1. Introduction

In the framework of the High Luminosity project of the Large Hadron Collider (HL-LHC), all the LHC injectors are undergoing an extensive upgrade program, named LHC Injector Upgrade (LIU) [1]. The first link of the heavy ion accelerator chain is represented by the Linac3 linear accelerator, Fig. 1, operating since 1994 [2]. As a part of the Linac3 upgrades, several activities involve the GTS-LHC Electron Cyclotron Resonance ion source (ECR), which produces the primary heavy ion beams [3]. The major efforts focus on the GTS-LHC extraction region, the double frequency plasma heating combined with afterglow operation [4] and the oven studies for metal ion beam production [5]. Concerning the oven studies, the lead ion beams delivered by the Linac3 are produced with the ECRIS using resistively-heated miniature ovens. Since the oven performance is related to the temperature distribution, a dedicated off-line test stand was built with the capability of measuring the oven temperatures and a numerical thermal model was developed to complement the measurements and evaluate the criticality of the several parameters involved. The application of the finite element method in the study of an ion source is a novelty in the accelerator community. In the following chapters the features of the advanced numerical method developed using the ANSYS Workbench finite element code [6] are described in detail, focusing the attention on the loading conditions, the material data and the assumptions adopted. The theoretical principles of the heat exchange are recalled to justify the assumptions taken. A benchmarking is performed between the numerical results and the experimental data in order to validate the numerical model. Finally, some recommendations are given for future and similar technologies and new solutions are proposed to improve the performance and service life of the source.

2. Component description

The GTS-LHC 14.5 GHz ECR ion source, Fig. 2, provides highly-charged heavy ion beams, predominantly lead, for the CERN experiments. The beam is generated from solid material evaporated in the ion source plasma chamber with resistively-heated ovens. The oven consists of a long vacuum-sealed stainless steel cane,[1] which contains a copper wire connected, at the end of the cane, to a tantalum heating filament wound around the crucible. The cane allows the axial insertion of the oven through the ion source injection plug, Fig. 3. The crucible is made of alumina, as well as the filament support and insulator. Finally, the crucible is positioned inside a tantalum shell which is connected to the cane, Fig. 4. The outer diameter of the oven is 14 mm and the total length, including the cane, is 870 mm, while the diameter of the tantalum filament is 0.45 mm. At the tip of the oven, two holes with a diameter of 1.5 mm and 5.5 mm in the crucible and the tantalum cover,

[1] This designation is technically used to identify the cylindrical shell containing the current lead.

* Corresponding author.
E-mail address: claudio.fichera@cern.ch (C. Fichera).

https://doi.org/10.1016/j.nima.2018.05.036
Received 8 January 2018; Received in revised form 26 March 2018; Accepted 15 May 2018
Available online 4 June 2018

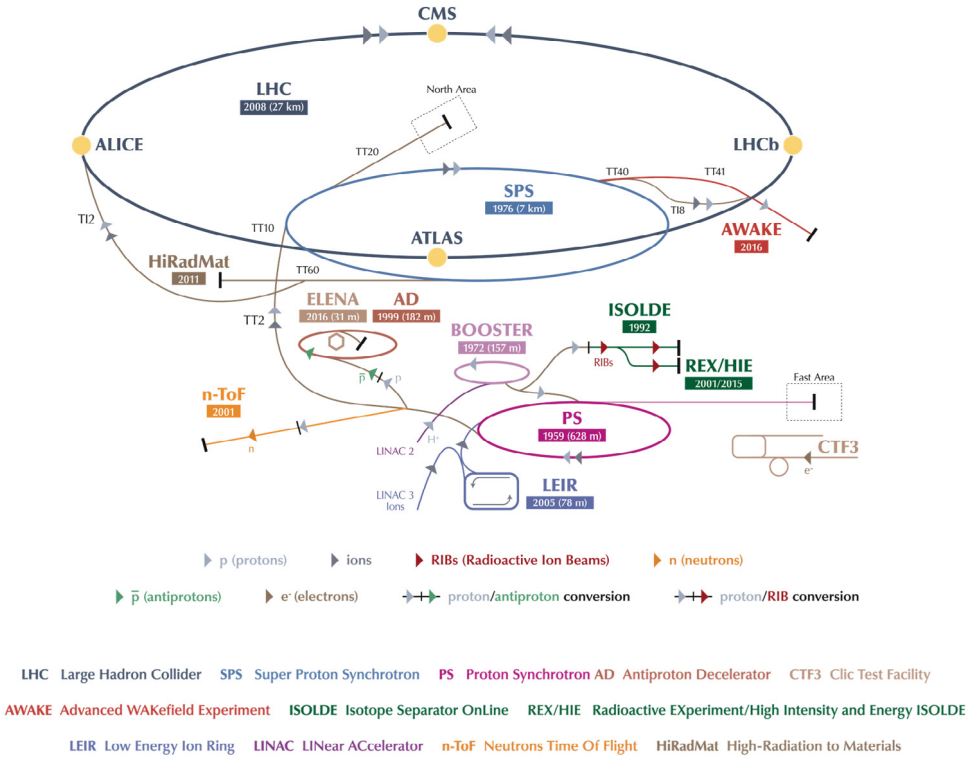

Fig. 1. The CERN accelerator complex.

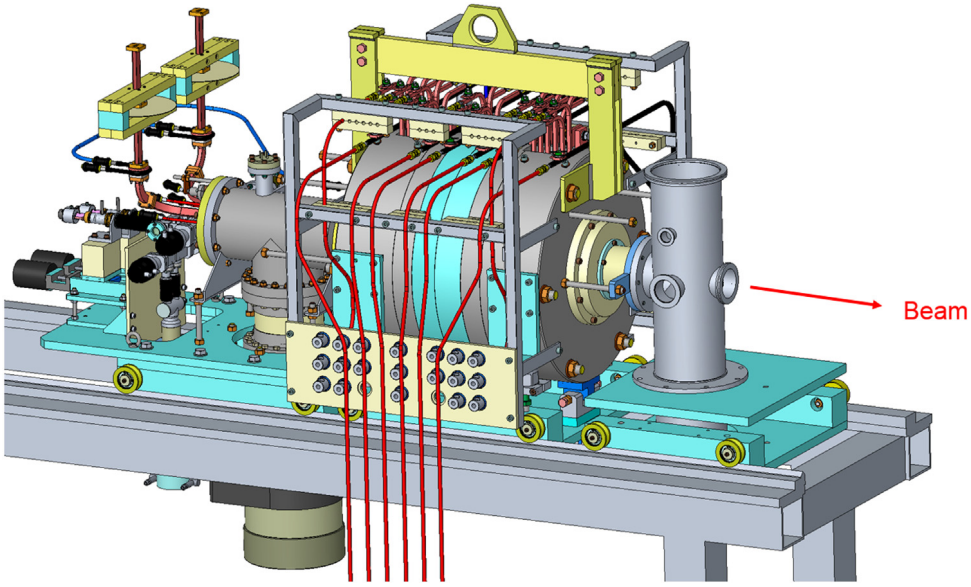

Fig. 2. Linac3 GTS-LHC ECR Ion Source (for clarity, the extraction vacuum pumps are not shown).

respectively, allow the evaporation of neutral atomic lead. The system can be dismounted to refill the crucible.

The crucible refilling is required every 2–3 operating weeks due to degrading beam performance. In some instances, the beam production is interrupted by blockage of the oven tip, either by formation of lead oxide or droplets of metallic lead [5]. These issues could be provoked by non-homogeneous temperature distribution along the crucible or temperature gradients in the neutral lead exit zone. In that sense, the thermal analysis of the system should provide further details about the oven behaviour.

3. Experimental measurements

A dedicated off-line test stand was built at CERN for monitoring the behaviour of the oven during the heating process, acquiring the most relevant physical quantities, such as the temperature in fixed points and the lead evaporation rates [5]. In particular, the oven was equipped with vacuum-grade thermocouples in order to measure the internal and external temperature. The thermocouple measuring the temperature inside the oven was secured to a copper pin 23 mm long with a diameter of 3 mm. The copper pin is inserted inside the alumina crucible and

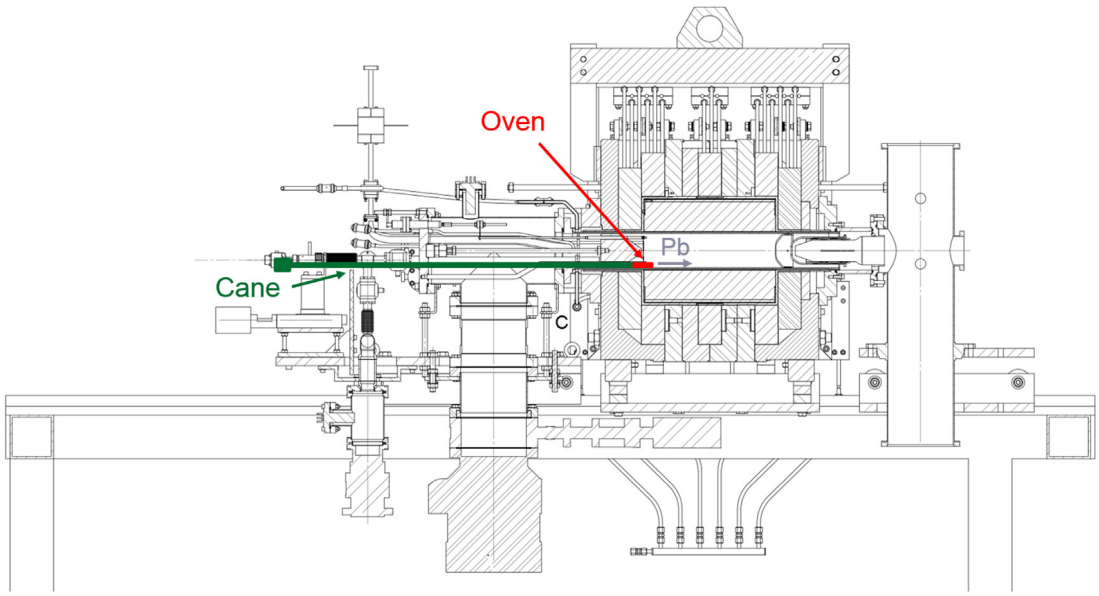

Fig. 3. Cross section of the Linac3 GTS-LHC ECR Ion Source.

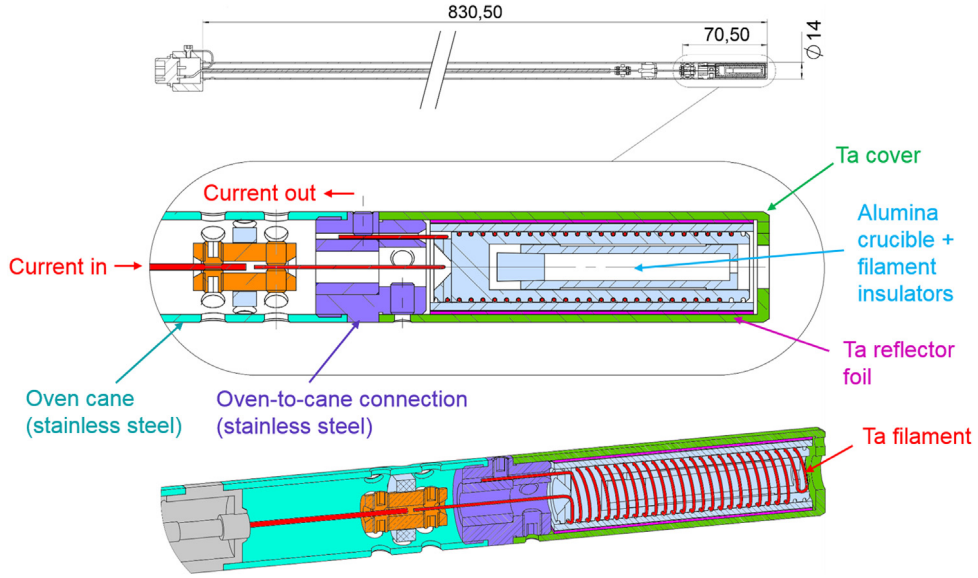

Fig. 4. GTS-LHC resistively-heated miniature oven.

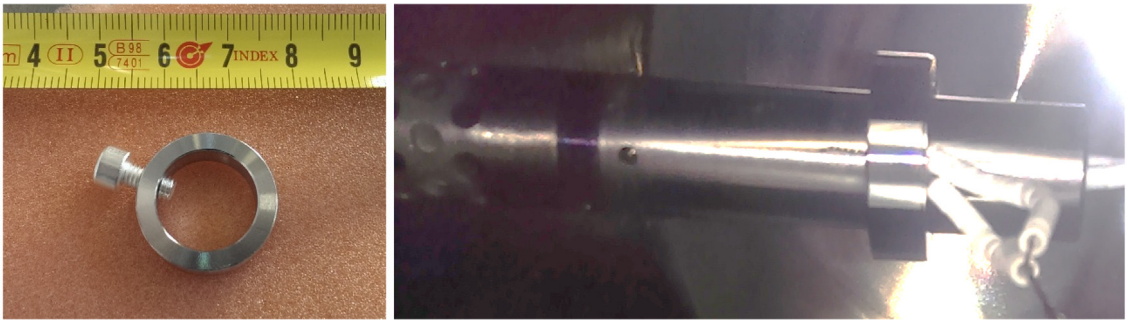

Fig. 5. *(Left)* Stainless steel holder ring for thermocouple installation and *(right)* setup for oven temperature measurements.

replaces the lead in order to perform measurements up to 1000 °C. On top of that, an additional thermocouple was attached to the outside surface of the tantalum shell, placed at the axial location corresponding to the centre of the crucible. In this case, the thermocouple was fixed

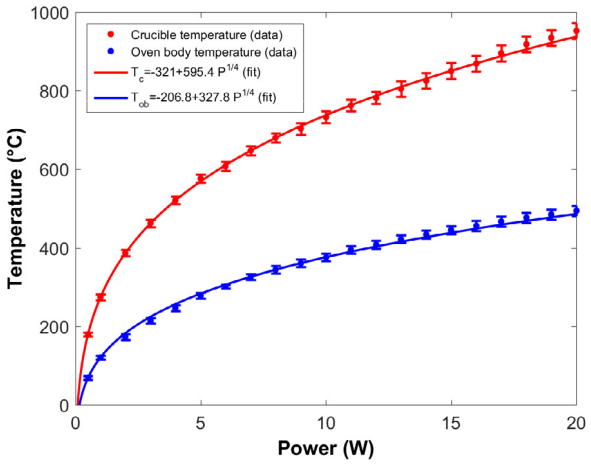

Fig. 6. Measured temperature vs. oven power: crucible (*red solid line*) and oven body temperature (*blue solid line*). (For interpretation of the references to colour in this figure legend, the reader is referred to the web version of this article.)

with a clamping system made of a stainless steel ring and a central screw, as shown in Fig. 5. In normal operation, the oven heating power is limited to 20 W. In Fig. 6, the experimental temperatures are reported as a function of the heating power in steady-state conditions.

For the production of lead beams, the oven is normally operated with power levels above 6 W. One can observe that the measured oven temperatures follow a $T \propto P^{1/4}$ relationship, where P is the power to the oven. Usually, this behaviour is typical of thermal radiation problems, as will be shown in the following section.

4. Heat transfer mechanisms

The heat transfer mechanisms governing the system under study were examined in detail to determine the most appropriate material parameters and boundary conditions for the thermal analysis. The conservation of energy specifies that net exchange of the energy of a system is always equal to the net transfer of energy across the boundary system as heat and work; applying this to a differential volume and considering the time variable t, the heat equation assumes the following differential form:

$$\rho c_p \frac{\partial T}{\partial t} - k\nabla^2 T = Q \tag{1}$$

The first term represents the transient part in which the energy is released or stored, where c_p is the specific heat capacity and ρ is the density. The second term is the temperature variation along the component, where k is the thermal conductivity and ∇^2 the Laplace operator, $\left(\frac{\partial^2 T}{\partial x^2} + \frac{\partial^2 T}{\partial y^2} + \frac{\partial^2 T}{\partial z^2}\right)$ in Cartesian coordinates, while Q is the internal heat generation rate per unit volume. The material properties are a function of the temperature. The heat equation is a partial differential equation that describes the distribution of heat (or variation of temperature) in a given region over time. In some cases, exact solutions of the equation are available; in other cases the equation must be solved numerically using computational methods. In a steady-state case, the thermal gradient is constant with time, $\frac{\partial T}{\partial t} = 0$ and Eq. (1) simplifies to:

$$-k\nabla^2 T = Q \tag{2}$$

In this work it is assumed that, both in the measurements and in the simulations, the steady-state condition is reached and (2) applies.

The exchange of energy in the system is regulated by the combination of three fundamental modes of heat transfer: conduction, convection and radiation.

4.1. Conduction

In the heat exchange by conduction, the internal heat transfer occurs between two points of the same body or two bodies in contact. The temperature gradient on a body in steady-state conditions follows the definition in (2). In the case of two bodies in contact, such as A and B in Fig. 7, the thermal flux between two points is:

$$q_x = -\frac{T_1 - T_2}{\frac{\Delta x_A}{k_A \cdot S} + \frac{1}{h_c \cdot S} + \frac{\Delta x_B}{k_B \cdot S}} \tag{3}$$

where S is the contact area, x the orthogonal direction, Δx_A and Δx_B the distances of the measuring points *1* and *2* from the interface. The thermal flux thus depends on the geometry of the bodies, on their thermal conductivity and on the coefficient h_c, which is called thermal contact conductance. This parameter is of paramount importance in the case of heat exchange between two good conductors, where most of the temperature gradient is often generated at the interface. The contact conductance is influenced by many factors, the contact pressure being the most important. The influence of the contact pressure on the thermal contact conductance has been widely discussed by many authors [7,8] and their relationship is typically expressed as follows:

$$h_c = 1.25 k_s \left(\frac{m}{\sigma}\right)\left(\frac{P}{H_e}\right)^{0.95} \tag{4}$$

where k_s is the harmonic mean of the thermal conductivities, σ is the roughness and m the related surface slope, while P is the contact pressure and H_e the effective elastic micro-hardness. Considering the system under study, most of the bodies in contact have a very low contact pressure, comparable to that generated by their deadweight, and the contribution of thermal conduction in the heat exchange between bodies in contact is expected to be negligible with respect to the heat exchanged by radiation (see Section 6.3).

4.2. Convection

Convection is the thermal exchange between a body and a surrounding fluid in motion. The basic relationship for the convection heat transfer is defined by the Newton's law of cooling:

$$q = hA\left(T_s - T_f\right) \tag{5}$$

where q is the heat flow between the body surface and the fluid, A the body surface in contact with the fluid, h the thermal convection coefficient and T_s and T_f are the absolute body surface and fluid temperatures, respectively. On the basis of the fluid motion, the convection may be classified as free (or natural) or forced. In the forced case, an artificially-induced convection current is created when a fluid is forced to flow around the body surface by means of an external source, such as a pump. In the case of natural convection, an increase of the temperature produces a reduction in the fluid density, which in turn causes the fluid motion.

In the system under study, the oven operates in vacuum and the convection contribution to the heat transfer is negligible.

4.3. Radiation

The thermal energy between two bodies is also exchanged through electromagnetic radiation. This mechanism is known as thermal radiation, because the random movement of atoms and molecules in a body, composed of charged particles, results in the emission of electromagnetic waves, which carry energy away from the body surface. Unlike convection, thermal radiation occurs also under vacuum. The transfer of radiant energy is described by the Stefan–Boltzmann's equation, which for two grey-body surfaces can be written as follows:

$$Q = \frac{\sigma \cdot \left(T_1^4 - T_2^4\right)}{\frac{1-\epsilon_1}{A_1 \cdot \epsilon_1} + \frac{1}{A_1 \cdot F_{1\to 2}} + \frac{1-\epsilon_2}{A_2 \cdot \epsilon_2}} \tag{6}$$

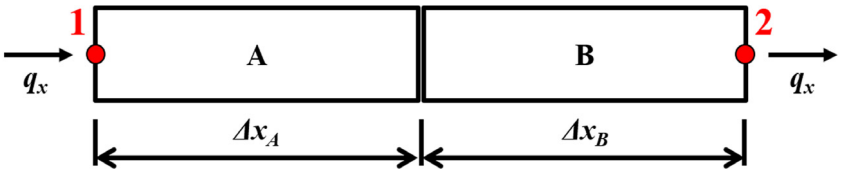

Fig. 7. Thermal flux between two solids in contact.

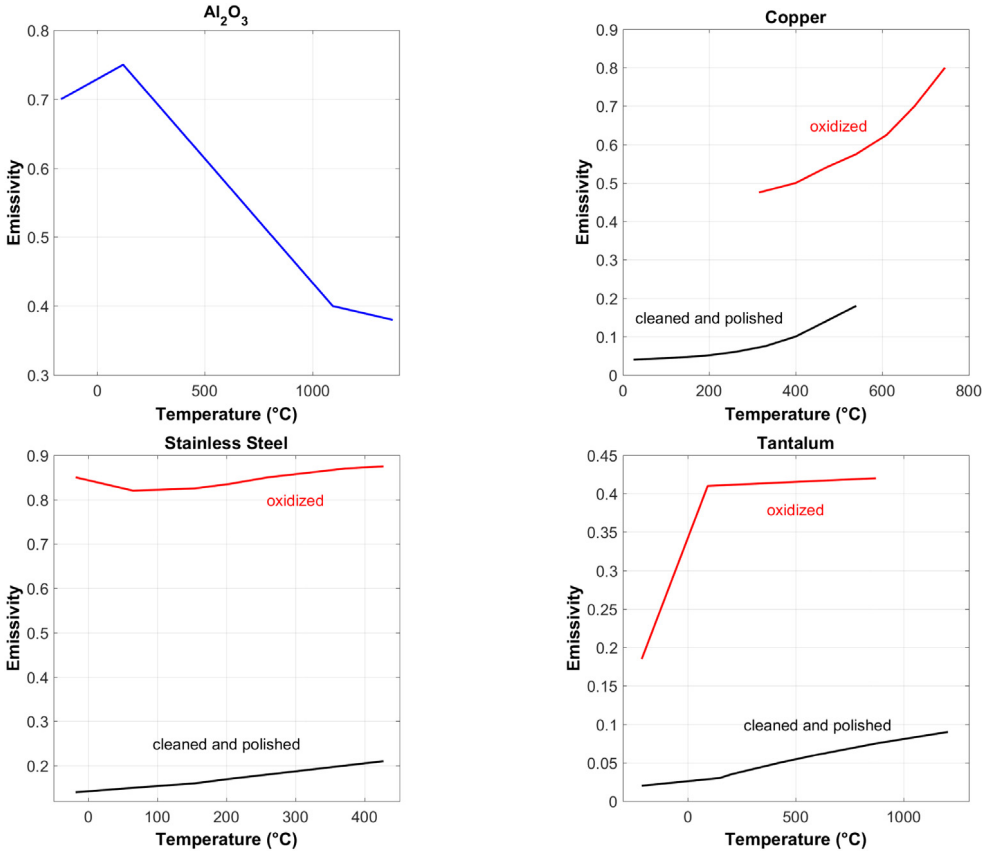

Fig. 8. Emissivity vs. temperature as a function of the surface state for: *(top left)* alumina (Al_2O_3), *(top right)* copper, *(bottom left)* stainless steel and *(bottom right)* tantalum [10,11].

where:

Q is the heat flux;

σ is the Stefan–Boltzmann constant;

$\epsilon_{1,2}$ are the emissivities of the surfaces 1 and 2 (equal to 1 for a black body);

$A_{1,2}$ are the surface areas 1 and 2;

$F_{1\to 2}$ is the shape factor;

$T_{1,2}$ are the absolute temperatures in Kelvin of surfaces 1 and 2.

In (6), only the emissivity depends on the material, while the other parameters are constant or depend on the geometry. The emissivity represents the material effectiveness in emitting thermal radiation and is generally measured as the ratio of the thermal radiation from a surface to the radiation from an ideal black body surface at the same temperature. The ratio varies from 0 to 1. Kirchhoff's law equates the emissivity of an opaque surface with its absorption of incident radiation. The largest absorptivity corresponds to complete absorption of all incident light by a truly black object, explaining why mirror-like and polished metallic surfaces that reflect light will thus have low emissivity. For several applications, when conduction and convection are present, radiation becomes relevant only at high temperatures. In the case under examination, radiation actually is the most relevant mechanism of heat exchange also at low temperatures, given the absence of the convection contribution and the low contact pressure between most of the components in contact, which minimizes the thermal exchange by conduction (see Section 6.3).

5. Materials

As seen in Section 4, the heat flow and the temperature gradient in steady-state conditions of the problem under study depend on the thermal conductivity and the emissivity of the materials. These properties are temperature-dependent, and available in literature for all the materials adopted in the analysis [9–11]. The emissivity, on the other hand, is strictly related to the surface state of the radiating bodies [10]. Fig. 8 shows the emissivity values for alumina, copper, stainless steel and tantalum as a function of temperature and surface state. It is important to underline that in the numerical analysis the data is linearly extrapolated for the higher temperatures. It is evident that, in general, the surface state consistently influences the emissivity. Nevertheless, the surface state can be challenging to assess accurately considering that it usually changes with time. The metal parts of the oven are machined without applying a finishing polishing and are then operated at high temperatures in a residual gas atmosphere with always some low level oxygen residue. Therefore, the surface conditions of the materials are expected to be between the polished and oxidized limits.

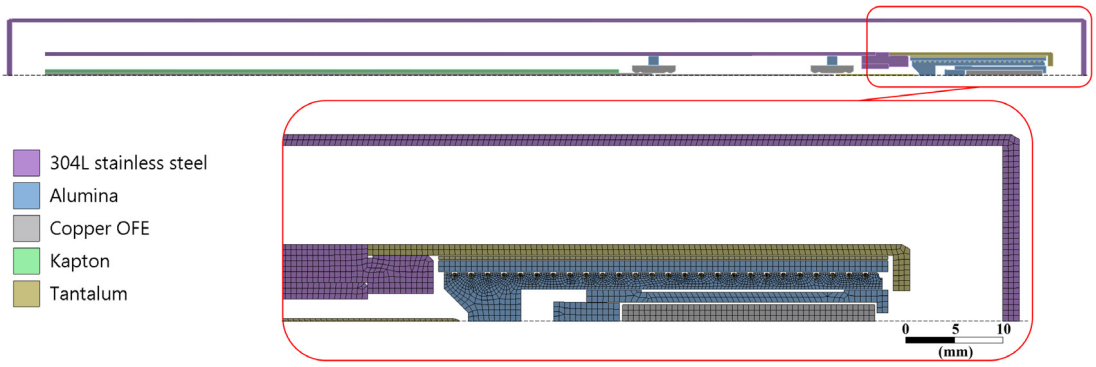

Fig. 9. 2D-axisymmetric model and materials.

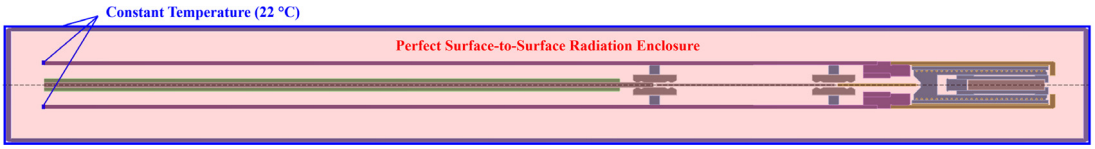

Fig. 10. Boundary conditions of the model.

6. Numerical model

6.1. Boundary conditions

Given the complex nature and nonlinearities of the problem, a finite-elements approach was adopted to model the system and the calculation was performed with ANSYS Workbench 17.2. In the simulation, the oven geometry was reproduced with a 2D-axisymmetric model and the cane length reduced to 250 mm, which is the length contained in the vacuum enclosure of the off-line test stand. Room temperature was imposed at the end of the stainless steel cane, as measured at the vacuum seal during oven heating. In addition, an external frame was created at 10 mm radial distance from the oven which directly exchanges heat with the surrounding ambient at the constant temperature of 22 °C, Fig. 9. It is important to highlight that the vacuum enclosure of the off-line test stand is roughly 50 mm around the oven; nevertheless, although the external frame in the model is much closer to the oven, the numerical results did not show significant difference moving it from 50 to 10 mm. The distance was set at 10 mm resulting in decreased calculation times.

The heat transfer between the components was modelled imposing a perfect surface-to-surface radiation, i.e. the total amount of energy exchanged inside a defined enclosure. In this case, the perfect enclosure is the whole area inside the simplified external frame, where surface-to-surface radiation occurs between the main system elements. In such enclosure the net total radiation is zero. The emissivity was imposed to the materials as a non-linear function of the temperature, according to the data from literature (Fig. 8). The boundary conditions are summarized in Fig. 10. Finally, the convection contribution was neglected for the reasons mentioned in Section 4, while the conduction through the thermal interfaces was estimated according to (3) (see Section 6.3).

6.2. Mesh

The model features about 7000 plane elements and the minimum edge length is 35 μm for elements in the filament region. For meshing, the *PLANE77* element of ANSYS was used, which is an 8-node thermal element with one degree of freedom at each node. Moreover, this element is well suited to model curved boundaries because quad/triangular-shaped elements may be formed. The mesh quality assessment was performed investigating the element quality function, which provides a composite quality metric that ranges between 0 and 1. This metric is based on the ratio of the volume to the sum of the square of the edge lengths for 2D elements. A value of 1 indicates a perfect square while 0 indicates that the element has zero or negative volume. In the present model, the element quality is over 0.9 for more than 6500 elements, i.e. 93% of the total.

6.3. Contacts

For most of the components in contact inside the oven, the pressure at the interfaces is very low and the body-to-body conductive heat transfer can be considered negligible with respect to the radiative one. Indeed, as shown in (4), for a low contact pressure the thermal conductance coefficient, h_c, approaches zero and, consequently, according to (3), the conductive heat flow approaches zero. The contact pressures were calculated considering the deadweight of the components. Nevertheless, in all cases, the thermal conductance coefficient is almost negligible (less than 0.1 W m^{-2} K^{-1}), except for the oven-to-cane bolted connection in stainless steel (see Fig. 11), for which a thermal conductance coefficient of 1 4500 Wm^{-2} K^{-1} was calculated assuming a tightening torque of 2 N m, which corresponds to 1 kN of axial force, between the two components with M12 thread.

6.4. Thermal loads

In normal operation the oven heating power is limited to 20 W and, based on the resistive power losses, one can estimate the power distribution in the different conductors (Tantalum (Ta), Copper (Cu) and stainless steel (SS)) as follows:

$$Powerratio = \frac{P_i}{P_{tot}} = \frac{P_i}{P_{Ta} + P_{Cu} + P_{SS}} \tag{7}$$

where:

$$P = R \cdot I^2 = \frac{\varphi \cdot l}{A} \cdot I^2 \tag{8}$$

P_i is either P_{Ta}, P_{Cu} or P_{SS}, while I is the current flowing through the conductors, as it is the same through all of them and thus disappears from the equation, the power ratios can be calculated. The conductors in the oven are: the tantalum filament, the copper wire inside the cane and the stainless steel cane which acts as a return conductor for current circuit.

Table 1
Power distribution ratios.

Conductor	Length l (mm)	Resistivity φ (nΩ m)	Cross section A (mm^2)	Power ratio
Ta filament	700	131	0.159	0.952
Cu wire	760	16.78	0.785	0.027
SS cane	760	690	40.84	0.021

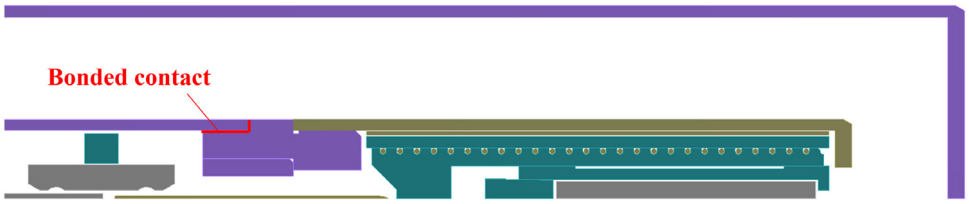

Fig. 11. Oven-to-cane bonded contact.

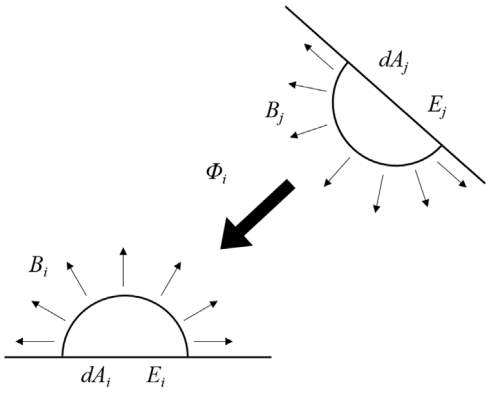

Fig. 12. Heat exchange between radiating bodies.

The rough estimation of the power distribution reported in Table 1 does not take into account the resistivity dependence with the temperature, but considers constant values at room temperature. On the other hand, most of the contribution to the total power comes from the tantalum filament, which results to it being the most heated and affected by the temperature increase. Taking into account that the resistivity usually increases as a function of the temperature, the relative contribution of tantalum to the total power would slightly further increase, approaching a value of 1. The error in the assumption of constant electrical resistivity with temperature is therefore less than 5%.

Considering the power distribution ratios in Table 1, the power is applied in the model as an internal heat generation (IHG) to each component. Six different thermal analyses were performed, with power varying from 1 to 20 W; the power has been distributed in the conductors as reported in Table 2.

6.5. Solution algorithm

It is of interest to detail the numerical method adopted by the finite element code to solve the thermal problem. As described above, the thermal radiation is the main heat transfer mechanism between different bodies. Radiation analyses are highly nonlinear, with the flux varying with the fourth power of the body's absolute temperature, as seen in Eq. (6), and the iterative solution is based on a convergence criterion. The *radiosity solver method* is well suited for generalized radiation problems in 2D/3D involving two or more radiating surfaces. In ANSYS, this method can be used for either transient or steady-state thermal analyses. The radiosity solver method is based on the heat exchange between radiating bodies by solving for the outgoing radiative flux for each surface, when the surface temperatures for all surfaces are known. Considering two radiating surfaces i and j, Fig. 12, the energy leaving the unit area dA in all directions is B, therefore the total energy leaving the surface i ($B_i \cdot dA_i$) can be divided into its own radiant component and the diffuse reflection of the radiance coming from other surfaces.

The total radiant energy corresponds to (6), simplifying the emission density E_i multiplied by the unit area ($E_i \cdot dA_i$). The diffuse reflection is the multiplication of the diffuse coefficient Φ_i and the part of energy coming from other surfaces which reaches the surface i. Integrating the contribution of all surfaces, the formula of the radiosity of the surface i is the following:

$$B_i \cdot dA_i = E_i \cdot dA_i + \Phi_i \cdot \int B_j \cdot F_{ji} \cdot dA_j \tag{9}$$

where F_{ij} is the shape factor which determines the fraction of total energy leaving the surface j which reaches the surface i. The surface fluxes provide boundary conditions to the finite element model for the conduction process analysis. The heat conduction is governed by Fourier's law (1) and for steady state problems the solution only requires the knowledge of the thermal conductivity (2). When new surface temperatures are computed, due to either a new step or iteration cycle, new surface flux conditions are found by repeating the process. The surface temperatures used in the computation must be uniform over each element surface facet to satisfy the conditions of the radiation model.

7. Results

In order to benchmark the experimental data, different simulations were run at increasing heating powers. While the thermal conductivity of the components as a function of temperature is well known from literature, the emissivity is the main variable affecting the thermal distribution. The range of values for the emissivity of each component was narrowed through bibliographic research, however, the emissivity strongly depends on the material surface state, which is unknown *a priori*. Parametric simulations were thus performed as a function of the different emissivities, to investigate the thermal response of the system.

7.1. Case 1

In the first case study (*Case 1*), the surface state was considered polished and cleaned for all the components. The emissivities used, extracted from Fig. 8, are reported in Table 3.

In Fig. 13, the temperatures obtained experimentally and numerically at the probe positions are compared. It is possible to observe that the numerical results overestimate the temperature distribution inside and outside the oven.

Table 2
Power distribution in the conductors.

Conductor	Volume (mm^3)	Total power (W)					
		1	2.5	5	10	15	20
		Distributed power (W)					
Ta filament	112.4	0.952	2.380	4.760	9.520	14.280	19.040
Cu wire	270.1	0.021	0.053	0.106	0.212	0.318	0.424
SS cane	11728.4	0.027	0.067	0.134	0.268	0.402	0.536

Table 3
Material emissivities for *Case 1* [10,11].

Alumina		Tantalum		Stainless Steel		Copper	
T (°C)	ϵ	T (°C)	ϵ	T (°C)	ϵ	T (°C)	ϵ
−167	0.700	−212	0.020	−18	0.140	25	0.040
121	0.750	149	0.030	65	0.150	120	0.045
260	0.700	204	0.035	154	0.160	260	0.060
538	0.600	427	0.050	204	0.170	330	0.075
815	0.500	593	0.060	260	0.180	400	0.100
1093	0.400	871	0.075	316	0.190	470	0.140
1371	0.380	1204	0.090	427	0.210	540	0.180

Table 4
Material emissivities for *Case 2* [10,11].

Alumina		Tantalum		Stainless Steel		Copper	
T (°C)	ϵ	T (°C)	ϵ	T (°C)	ϵ	T (°C)	ϵ
−167	0.700	−212	0.185	−18	0.850	315	0.475
121	0.750	93	0.410	65	0.820	400	0.500
260	0.700	871	0.420	154	0.825	470	0.540
538	0.600			204	0.835	540	0.575
815	0.500			260	0.850	610	0.625
1093	0.400			316	0.860	675	0.700
1371	0.380			427	0.875	745	0.800

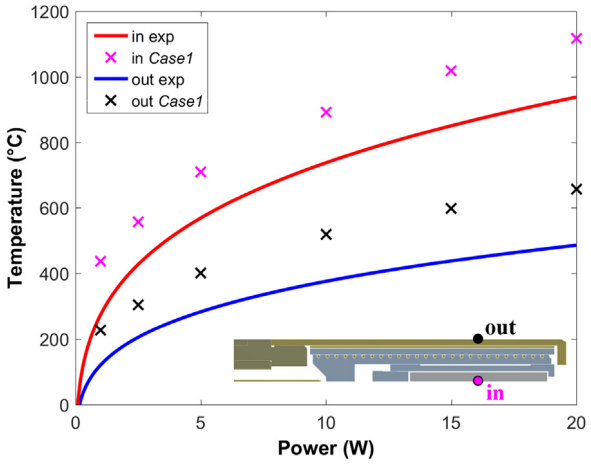

Fig. 13. Numerical-experimental comparison for *Case 1*.

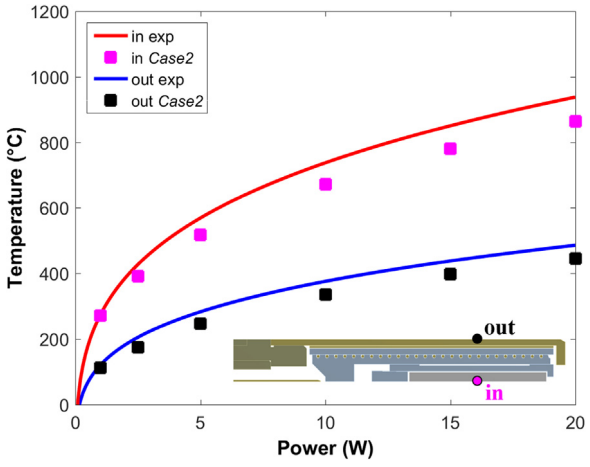

Fig. 14. Numerical-experimental comparison for *Case 2*.

7.2. Case 2

As opposed to *Case 1*, *Case 2* assumes heavily oxidized surfaces. The numerical results are much closer to the experimental measures, Fig. 14. The emissivities adopted are reported in Table 4.

The real scenario lays between the two extremes, *Case 1* and *Case 2*. In fact, even if the initial surface state of the components is measurable, the level of oxidation changes with time and heating cycles. Several simulations were performed with different emissivity values for the materials, depending on the different oxidation levels assumed. Sensitivity analyses showed that the results were mostly sensitive to the variation of the emissivity of tantalum. Out of the tens of different combinations simulated, two additional cases to *Case 1* and *Case 2* are reported in this work.

7.3. Case 3 and 4

Section 7.2, and in particular *Case 2*, shows that the assumption of oxidized materials well represents the behaviour of the oven in operation. While the exact grade of oxidation of the components is uncertain, one can deduce, looking at Fig. 14, that it is lower than what assumed in *Case 2*. A fine-tuning of *Case 2* was therefore performed in terms of emissivity of the tantalum, which resulted, out of the sensitivity study performed, the most influent parameter in the determination of the results. Two additional cases, with intermediate tantalum oxidation,

Table 5
Tantalum emissivities for different cases simulated.

Case 1		Case 2		Case 3		Case 4	
T (°C)	ϵ	T (°C)	ϵ	T (°C)	ϵ	T (°C)	ϵ
−212	0.020	−212	0.185	−212	0.080	−212	0.150
149	0.030	93	0.410	1204	0.200	1204	0.300
204	0.035	871	0.420				
427	0.050						
593	0.060						
871	0.075						
1204	0.090						

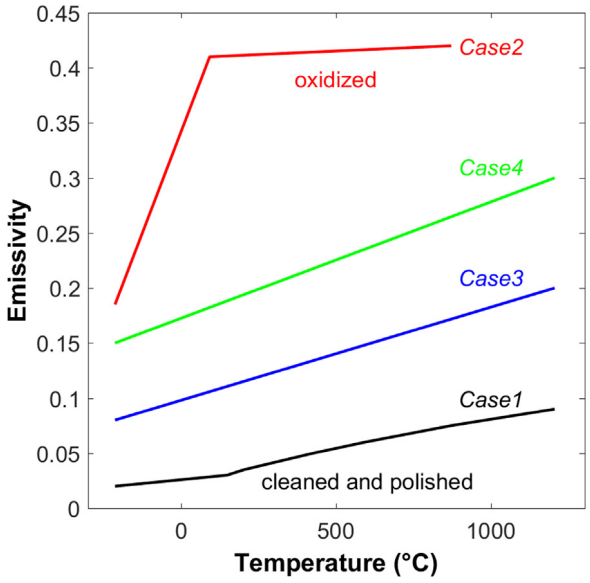

Fig. 15. Emissivity vs. temperature for tantalum in the different cases simulated.

Case 3 and *Case 4*, were run. For the new cases, a simple linear relationship between emissivity and temperature was assumed. The tantalum emissivities used in the four cases are reported in Table 5 and, for the sake of clarity, their difference is graphically shown in Fig. 15.

The results with the new ranges of the tantalum emissivity are shown in Fig. 16. In addition, the root-mean-square error (RMSE) for each case is reported in order to estimate the differences between the simulated results and the experimental measures. *Case 4* shows the best agreement with the experimental data. This scenario features an intermediate oxidation of tantalum which is also compatible with the visual inspections performed on the component.

Fig. 17 presents the calculated temperature distributions inside the oven with 15 W and 20 W heating powers. It is possible to observe that a rather good temperature uniformity is achieved along the crucible, while the tip of the oven remains significantly colder. At 20 W the temperature gradient between the material in the crucible (point 3) and the crucible tip (point 2) is about 45 °C, while between the crucible tip and the oven tip (point 1) it is about 420 °C. This relevant gradient between the inner and outer part of the oven can be further highlighted observing the heat flux in Fig. 18. Indeed, the heat flux is concentrated between the filament, i.e. the heating source, and the crucible confining most of the energy around the copper pin.

8. System optimization

The tantalum emissivity was found to be the most important parameter influencing the behaviour of the system. Nevertheless, the emissivity depends on the surface state, which changes during time due to oxidation. This effect can be taken into consideration introducing a relationship between time and emissivity for tantalum. In order to do so, the emissivity should be measured at different working times in the test bench oven, predicting the behaviour of the component during operation in the ion source. Of course, this method is effective if the initial emissivity and surface state of the tantalum used in the test bench and in the source are the same. In that sense, surface treatments, such as sandblasting or ion bombardment, can be effectively performed to impose the desired surface state to the component [12].

Moreover, the calculated temperature distribution inside the oven shows a good axial uniformity at different heating powers; nevertheless, the temperature drop in the oven tip has given the first hints to possible causes of the observed early reduction of the oven performance. Indeed, in normal operation the two ovens installed in the GTS-LHC provide 2–3 weeks of lead beam operation between refills. However, it was observed that when a refill is required due to degrading beam performance,

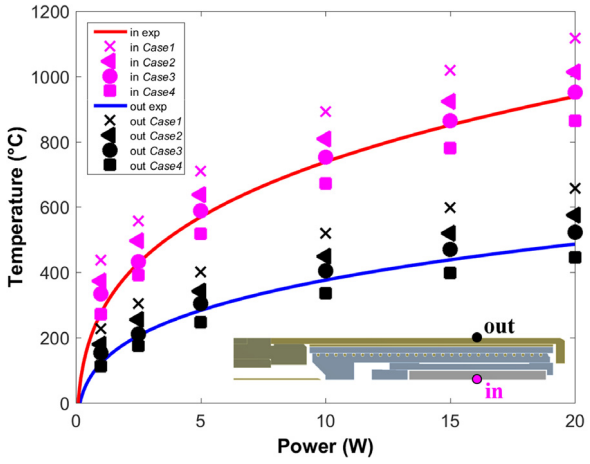

Case	RMSE (°C)
1	146.7
2	46.2
3	73.3
4	27.8

Fig. 16. Numerical-experimental comparison for cases *1* to *4*.

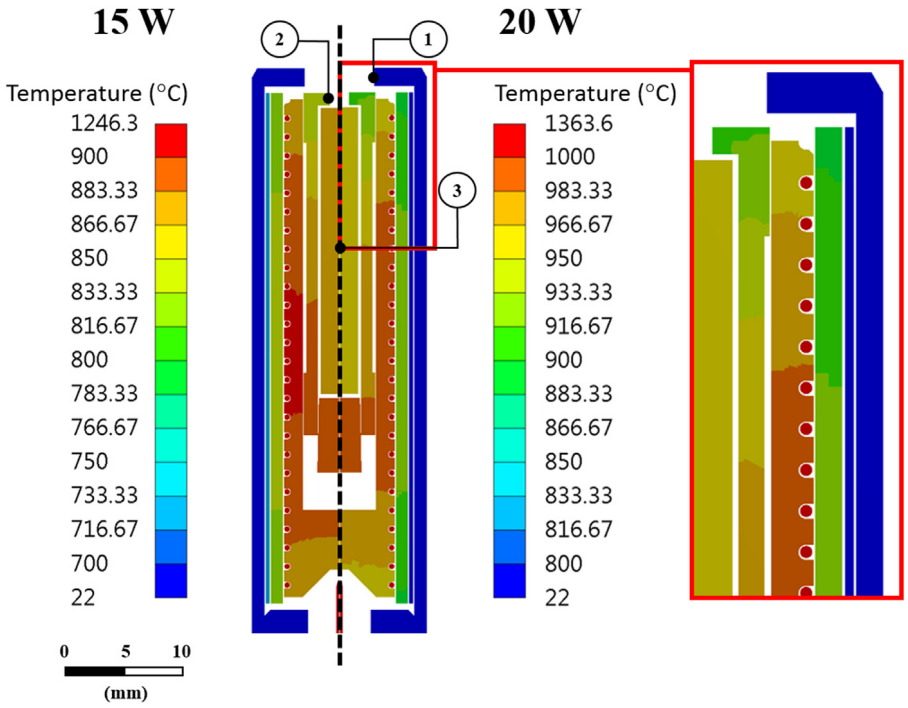

Fig. 17. *Case 4* model: simulated temperature distribution inside the GTS-LHC miniature oven with 15 and 20 W heating powers. The oven tip is at the top. Temperatures at locations 1, 2 and 3 are 482, 834 and 870 °C for the 15 W case and 536, 915 and 960 °C for the 20 W case.

typically about 2/3 of the lead is still left in the oven. In some cases the operation is also interrupted by blockage of the oven tip, either by formation of lead oxide or droplets of metallic lead which could be caused by the cold oven tip observed in the simulations. In order to reduce the temperature gradient in the oven tip, a possible solution could be to improve the filament winding around the crucible, exploiting all the available space, in particular close to the tip. Additionally, increasing the contact pressure between the components would enhance the heat transfer by conduction, facilitating the thermal diffusion and reducing the temperature gradients between the oven parts.

The effectiveness of these two last proposals was analysed by means of numerical simulations. Concerning the filament winding, the oven geometry was modified extending the filament support in order to exploit all the free space close to the oven tip (Fig. 19 *centre*). Instead, the enhancement of the thermal diffusion by conduction was simulated setting a perfect contact between the tantalum reflector foil and the oven cover. In Fig. 19 the temperature distribution obtained at 10 W in these two cases is compared with what obtained with the baseline of *Case 4*.

The comparison shows that the extension of the filament support up to the tantalum cover slightly modifies its temperature distribution with respect the original oven geometry. However, this solution has no relevant effect on temperature along the crucible and, in particular, on the temperature gradient in the oven tip, which is about 315 °C as in the baseline case. On the other side, enhancing the thermal conduction between the reflector foil and the oven cover has a relevant influence on the thermal behaviour of the system. Indeed, the first evident result is the drop-off, by about 60 °C, of the temperature in the inner side of the oven; nevertheless, the temperature uniformity is maintained along the crucible. This effect is complemented by a temperature increase of about 30 °C in the tantalum cover due to the thermal diffusion between the reflector foil and the cover. The temperature gradient in the oven tip is reduced to 230 °C, 30% less than the gradient of the baseline case.

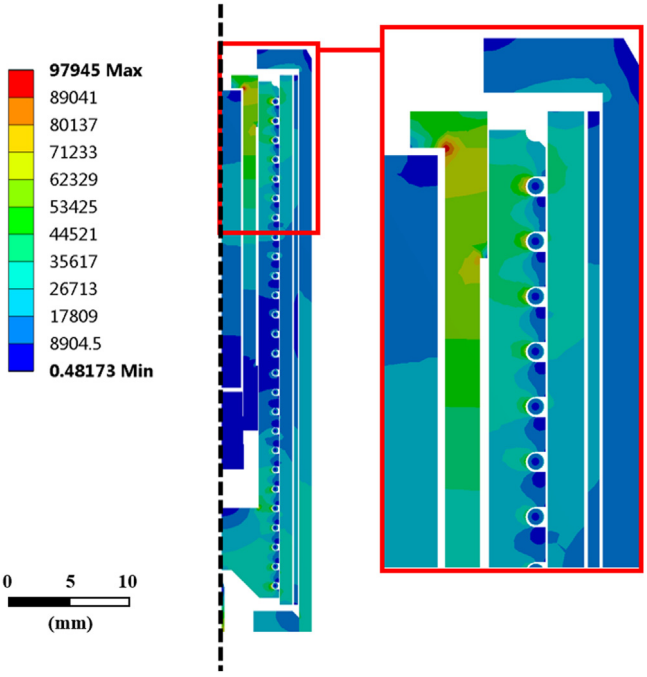

Fig. 18. *Case 4* model: heat flux (W m^{-2}) at 20 W heating power.

9. Conclusions

An advanced numerical study was performed with the finite-elements method to evaluate the temperature distribution in the miniature ovens installed in the Linac3 GTS-LHC ECR ion source and assess the thermal behaviour of the system, which strongly influences the operational performance of the component. The thermal radiation was determined to be the main contribution to the heat exchange between the oven parts. The numerical model was benchmarked with measurements taken in an offline test stand which reproduces the same environment and thermal system of the ion source. The numerical

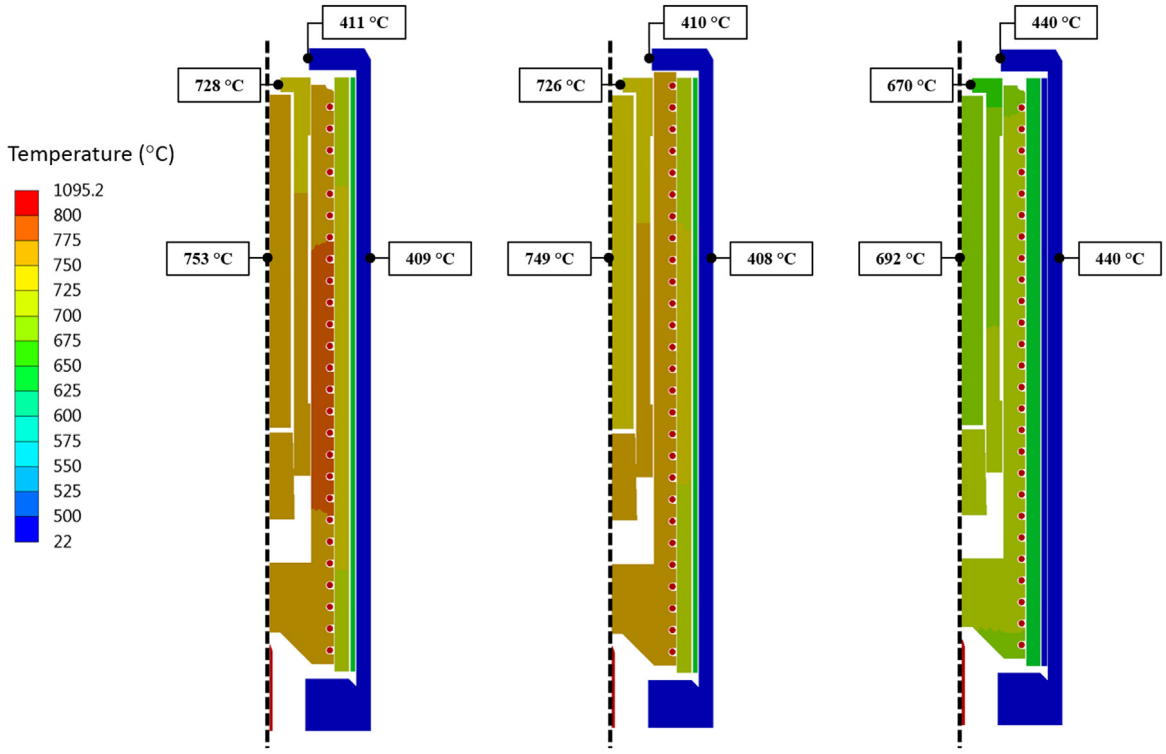

Fig. 19. Temperature distribution of different numerical simulations at 10 W oven power: *(left)* actual oven geometry radiation dominated, *(centre)* modified geometry exploiting the available space close to the oven tip and *(right)* actual oven geometry with the tantalum reflector foil in contact with the oven cover.

simulations provided good agreement with the experimental data and, analysing the results, the tantalum emissivity turned out to be the crucial parameter influencing the behaviour of the system. Since the emissivity depends on the surface state, a satisfactory numerical-experimental benchmarking was obtained assuming intermediate conditions in terms of tantalum oxidation. Proposals to improve the thermal performance of the system were discussed considering the experimental observations and numerical outcome. Numerical simulations shown that introducing the thermal conduction between bodies allows to improve the temperature distribution of the system and, consequently, the service life of the source. Finally, the results obtained allowed to pinpoint general guidelines which could be beneficial also for similar systems and technologies. First of all, it is fundamental to assess and control the surface state of the components at the beginning of their life, and evaluate the evolution of the oxidation of the equipment during operation. Moreover, the emissivity of the adopted materials has to be carefully measured as a function of the surface state and oxidation on material samples. Finally, in order to obtain a more accurate model validation and monitor the temperature gradients along the structure components, the data acquisition system in dedicated test benches should feature an increased number of measuring points.

References

[1] G. Apollinari, et al. High-Luminosity Large Hardon Collider (HL-LHC): Preliminary Design Report, Rep. CERN, CERN-2015-005, 2015.
[2] H.D. Haseroth, Pb injector at CERN, in: Conf. Proc. C9608262, vol. 1, 1996, pp. 283–287.
[3] L. Dumas, et al. Operation of the GTS-LHC source for the hadron injector at CERN, in: Proc. of ECRIS 2006, Lanzhou, China, Published in HEP & NP, vol. 31, suppl. 1, 2007, pp. 51–54. Also available as LHC Project Report 985.
[4] V. Toivanen, et al., Effect of double frequency heating on the lead afterglow beam currents of an electron cyclotron resonance ion source, Phys. Rev. Accel. Beams 20 (2017) 103402.
[5] V. Toivanen, et al. Recent developments with the GTS-LHC ECR ion source at CERN, in: Proc. of ECRIS 2016, Busan, Korea.
[6] ANSYS Workbench User's Guide, Release 15.0, 2013.
[7] E.E. Marotta, et al., Thermal joint resistance of polymer-metal rough interfaces, J. Electron. Packag. 128 (2006) 23–29.
[8] M.G. Cooper, et al., Thermal contact conductance, Int. J. Heat Mass Transfer 12 (1969) 279–300.
[9] J.H. Lienhard IV, J.H. Lienhard V, A Heat Transfer Textbook, fourth ed., Phlogiston Press, 2016.
[10] W.D. Wood, et al., Thermal Radiative Properties, in: Plenum Press Handbooks of High-Temperature Materials, vol. 3, 1964.
[11] E.A. Avallone, T. Baumeister III, Marks' Standard Handbook for Mechanical Engineers, McGraw-Hill, New York, NY, 1978, pp. 63–79.
[12] Z. Sobiech, et al. Cooling of the LHC injection kicker magnet ferrite yoke: measurements and future proposals, in: Proceeding of IPAC 2014, Dresden, Germany, 2014, pp. 544–546.